White-emission from ZnS:Eu incorporated in AC-driven electroluminescent devices via ultrasonic spray pyrolysis

Rivera-Medina, Martha Judith; Carrillo-Verduzco, Angélica; Rodríguez-Gómez, Arturo; Loi, Maria Antonietta; Alonso-Huitrón, Juan Carlos

Published in:
Materials Chemistry and Physics

DOI:
10.1016/j.matchemphys.2021.124866

Publication date:
2021

Materials Chemistry and Physics 270 (2021) 124866

Contents lists available at ScienceDirect

Materials Chemistry and Physics

journal homepage: www.elsevier.com/locate/matchemphys

White-emission from ZnS:Eu incorporated in AC-driven electroluminescent devices via ultrasonic spray pyrolysis

Martha Judith Rivera-Medina [a,b], Angélica Carrillo-Verduzco [a], Arturo Rodríguez-Gómez [c], Maria Antonietta Loi [b], Juan Carlos Alonso-Huitrón [a,*]

[a] Instituto de Investigaciones en Materiales, Universidad Nacional Autónoma de México, Ciudad Universitaria, A.P. 70-360, Coyoacán, 04510, Mexico City, Mexico
[b] Zernike Institute for Advanced Materials, University of Groningen, Nijenborgh 4, 9747, AG Groningen, the Netherlands
[c] Instituto de Física, Universidad Nacional Autónoma de México, Ciudad Universitaria, A.P. 20-364, Coyoacán, 04510, Mexico City, Mexico

HIGHLIGHTS

- White-emitting-AC-thin film electroluminescent device has been achieved using only europium doped ZnS as phosphor layer.
- The electroluminescent device with a MISIM architecture was fabricated by low-cost ultrasonic spray pyrolysis technique.
- The use of ZrO_2 insulator layers promotes the incorporation of Eu^{3+} and point defects at the phosphor-insulator interfaces.
- The white emission comes supposedly from electron-impact excited Eu^{2+}, Eu^{3+}, and defects at the phosphor-insulator interface.
- The white emission of the electroluminescent device is close to that of a standard illuminant.

GRAPHICAL ABSTRACT

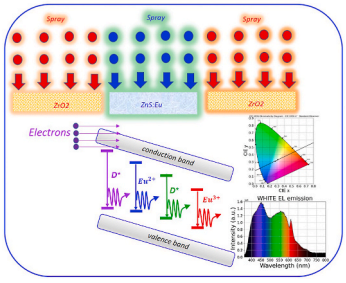

ARTICLE INFO

Keywords:
White-electroluminescence
Europium impurities
ZnS thin films
ZrO_2 thin films
Interfacial properties
Electroluminescence mechanisms
Colorimetry

ABSTRACT

In this work, white-emitting-alternating-current-thin film electroluminescent (w-ACTFEL) devices are demonstrated using europium-doped zinc sulfide (ZnS:Eu) and zirconium oxide (ZrO_2) as the emissive and dielectric layers, respectively. These films were deposited by the ultrasonic spray pyrolysis technique on antimony-doped tin oxide glass substrates, forming a standard metal-insulator-semiconductor-insulator-metal (MISIM) architecture. 10 kHz sinusoidal voltages activated the white-EL of the devices. The colorimetric characteristics were investigated for three amplitudes of the applied voltage. The emission of the devices is made up of wide and narrow bands with peaks corresponding to violet, blue, green and red light, which together produce the resulting white light. According to the colorimetric analysis, this white light is close to the standard D65 CIE illuminant with a minimal dominant blue component. The variation in voltage amplitude induces small changes in the visual characteristics of the EL emission. The white-EL emission of these MISIM devices is attributed to the

* Corresponding author.
E-mail address: alonso@unam.mx (J.C. Alonso-Huitrón).

https://doi.org/10.1016/j.matchemphys.2021.124866
Received 26 April 2021; Received in revised form 16 June 2021; Accepted 18 June 2021
Available online 22 June 2021

electron-impact excitation and subsequent relaxation of the excited levels of Eu^{2+} and Eu^{3+} impurities, and defect levels in the sublayer regions adjacent to the ZrO_2–ZnS:Eu interfaces.

1. Introduction

There is increasing interest in developing new approaches to fabricate white and multicolored electroluminescent (EL) devices operated by alternating current (AC) and direct current (DC) as light sources, displays, and sensing [1–7]. DC-driven EL devices have been established as bright and efficient light sources from a variety of materials as organic semiconductors (OLEDs) [8], III-V semiconductors [9], and colloidal quantum dots (QLEDs) [10]. However, AC-driven EL (ACEL) devices have recently gained considerable attention as promising alternatives to DC-driven devices, because they do not require of AC/DC converters and other costly switching devices which introduces power losses and complicated back-end electronics [11–14]. Furthermore, their intrinsic ability of flexible and straightforward device architecture with uniform large light-emitting areas with low heat generation and power consumption are further reasons of interest [15,16]. Among the different structures developed for ACEL devices, inorganic thin-film ACEL (ACTFEL) with a MISIM (metal-insulator-semiconductor-insulator -metal) architecture have been successfully used in monochromic flat panel displays for applications where it is required to stand extreme conditions, such as high temperatures, strong vibrations, and environments with high humidity [1,17–20]. ZnS doped with transition metals and rare-earth ions has served as an excellent semiconductor phosphor material for multiple ACEL devices with single emissions spanning the entire visible spectrum [21–24]. An outstanding example is the bright yellow-orange luminance from ZnS:Mn in ACTFELs [25–27]. Moreover, ZnS has also shown green-blue photoluminescence ascribed to the intrinsic defects, namely zinc and sulfur vacancies which creates new energy states within the bandgap [28–30]. The fabrication of single color and full-color ACTFEL devices has been subject of interest for more than three decades; through the incorporation of rare earth (Eu, Tb, Sm, Tm, Ce) and transition metal ions (Cu, Ni) to ZnS and other metal-sulfide host semiconductor [20,21,31]. Vast majority of the pioneers multicolor ACTFEL displays were fabricated by atomic layer deposition (ALD), RF sputtering and electron beam evaporation using phosphors such as ZnS: Mn, ZnS:Eu, ZnS:Sm, Cl and CaS:Eu for red, ZnS:Tb, Cl for green, and ZnS:Tm,F and SrS:Ce for blue emission [19,20,32–34]. But, the luminance of the green - ZnS:Tb,F devices was around 33%, therefore below the luminance of those yellow-ZnS:Mn devices, while the luminance of devices with the red and blue phosphors was much lower. Regardless of the low luminance for monochromatic emission, efforts were made to fabricate white AC-TFEL displays; first, a co-doped system of Eu,Ce, K-doped SrS, second through a multilayered phosphors stack. In the former, a reducing agent, as H_2, was incorporated to enhance the crystallinity of the phosphor layer, which is crucial for the performance of an AC-TFEL [35]. Although the luminance of these films was high, the CIE coordinates were not given in this work. Other works reported CIE coordinates; $(x, y) = (0.41, 0.39)$ for similar SrS:Eu, Ce AC-TFEL devices with reddish-white emission [20,36]. In the latter, a high luminance was achieved with CIE coordinates $(x, y) = (0.42, 0.48)$ by stacking consecutive layers of ZnS:Mn and SrS:Ce. The white-emission was the result of combining the yellow and blue emission from each phosphor layer, respectively [20]. Yet this device involves additional processing steps since it requires the deposition of two different phosphor layers when compared with the SrS:Eu,Ce,K device. Other co-doping systems using SrS:Cu,F and SrS:Cu, Cl AC-TFEL prepared by electron beam/-thermal multi-source evaporation and hot wall deposition show a whitish-blue emission with chromaticity coordinates, $(x, y) = (0.25, 0.27)$ and $(x, y) = (0.19, 0.28)$, respectively [37,38]. In these works, the EL spectrum exhibits a broadening and a more prominent contribution of the red edge than the blue PL spectrum of the SrS:Cu phosphor, which gave more evidences of the differences between the PL and EL mechanisms demonstrated in an earlier work [39].

Despite of all these research activities, the challenge of developing low-cost approaches for the fabrication of white-multicolor ACTFEL displays, remains.

In this work, we demonstrate white light EL from MISIM AC-TFEL devices fabricated using ZnS:Eu as phosphor layer and ZrO_2 as dielectric layers deposited by ultrasonic spray pyrolysis, which is a low-cost and relatively fast and straightforward technique. It does not require high vacuum equipment, neither require post-annealing processes. The colorimetric characteristics of this device are explored and the emission mechanisms are also analyzed and discussed in this work.

2. Materials and methods

2.1. Ultrasonic spray coating conditions and fabrication of AC-driven devices

The schematic diagram of the fabricated MISIM device is shown in Fig. 1. We used a home-made ultrasonic spray coater to deposit layer-by-layer in one step process our AC-driven device. Details of our system can be found elsewhere [40]. An oil-free air compressor provided the transporting gas for all of our experiments. Approximately one-third of the ATO (antimony doped tin oxide) covered substrate was covered with a microscope slide to prevent film formation upon upcoming device layers. The thin film of ZnS:Eu (emissive thin film) was grown at 420 °C using a carrier and directional gas flow of 2.0 l min^{-1} and 0.8 l min^{-1}, respectively. The emissive layer was sandwiched between two dielectric layers of ZrO_2. The starting solution for the dielectric film of ZrO_2 consisted of 0.05 M of zirconium (IV) acetylacetonate dissolved on a mixture of anhydrous methanol and diethylene glycol monobutyl ether in a 9:1 ratio. The deposition time of this film was 3 min, which led to a film thickness of 150 nm. The bottom dielectric layer was directly grown on top of the ATO substrate while the top dielectric layer was treated differently before starting the film by flushing air for 30 s through the directional flow duct. Finally, aluminum (purity of 99.999%) electrodes with a thickness of 100 nm were thermally evaporated (5–6 x 10^{-6} Torrs) using a shadow mask. The active area of our AC- driven devices was determined by the radius of the rear electrode (1 mm).

2.2. Characterization of thin films and MISIM device

The crystalline structure of the ZnS:Eu and ZrO_2 films were determined by X-ray diffraction measurements using a Bragg-Brentano ULTIMA IV diffractometer with an X-ray source of Cu Kα line (0.15406 nm) at a grazing beam configuration angle of 1°. Cross-sectional scanning electron micrographs were obtained using a field-emission ultrahigh-resolution Scanning Electron Microscope JEOL- JSM-7800F. Before the observation, the samples were manually polished using a tripod polisher

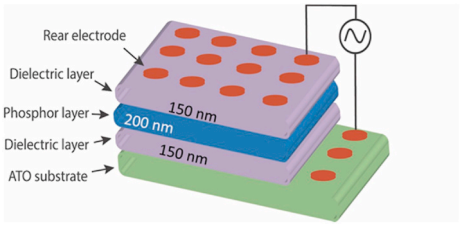

Fig. 1. Illustration of the AC-TFEL- MISIM structure fabricated by ultrasonic spray pyrolysis.

(South Bay Technology model 590 TEM). The ACTFEL-MISIM devices were driven by applying 10 kHz sinusoidal voltages using a Wavetek function generator, model 182A, and a step-up transformer. The peak to peak voltages were measured using a Hewlett Packard/1741 oscilloscope. The EL signal was collected with a quartz optical fiber, and the emission spectra were recorded, in the range from 350 to 800 nm, using a Spex Fluoromax spectrofluorometer. The emitting properties of the EL devices were measured in dark ambient conditions at room temperature.

3. Results and discussion

Fig. 1 shows the schematic diagram of the fabricated MISIM device.

The X-ray diffraction pattern of the ZnS:Eu film used in the MISIM structure is shown in Fig. 2. According to this pattern and the card number 01-084-3995 from the PDF-2-(2004) database, the film is polycrystalline. All the peaks correspond to the hexagonal wurtzite crystalline phase of ZnS, and there is a preferential orientation at $2\theta = 28.6^{\circ}$ and a secondary diffraction peak at $2\theta = 51.9^{\circ}$, which correspond to the (002) and (103) planes, respectively. Since Eu is only included as an impurity at a low doping level, its incorporation in the ZnS matrix could not be verified by XRD. The evidence of the Eu doping into the ZnS lattice of these films was given in a previous work by means of electron spin resonance (ESR) measurements [40]. The inset of Fig. 2 shows the XRD pattern of the ZrO_2 thin films used in the MISIM device. According to the JCPDS card 50–1089 the 2θ positions of all the diffraction peaks correspond to the polycrystalline tetragonal phase of ZrO_2. In both cases, the average crystallite size was obtained from the full width at half maximum of the main diffraction peaks and using the Debye-Scherrer formula, without taking into account stress or other effects. Considering the two main XRD peaks of the ZnS: Eu film and the four XRD peaks of the ZrO_2 film, the average crystallite sizes were, D = 23.5 nm ± 1.4 nm, and D = 3.9 nm ± 0.8 nm, respectively.

Fig. 3 Shows the cross-section SEM image of the MISIM - ATO/ZrO_2/ZnS:Eu/ZrO_2/Al structure. This SEM image illustrates the fact that the dielectric or phosphor layer and the interfaces of the as-deposited MISIM device, generally contain imperfections, such as pinholes, impurities, particulates, and substrate non uniformities. Since these imperfections cause micron and submicron-sized weak spots, which are susceptible to catastrophic breakdown at the voltages required for regular operation, we carried out a self-healing electrical process [36,41], before obtaining the EL spectra shown in Fig. 4. The healing process given to the MISIM-EL devices consisted of applying increasing rms-voltages in steps of 10 V for 10 min, from 0 V to the threshold voltage. We proved that it was an effective self-healing electrical process because the EL devices operated without this process suffered from light emission instability and sparks, and catastrophic breakdown at relatively low voltages.

Fig. 4 shows the EL spectra of the ATO/ZrO_2/ZnS:Eu/ZrO2/Al - MISIM structure for three rms-voltages; $V_1 = 56V$, $V_2 = 70V$ and $V_3 = 77\ V$, in the spectral region from 350 to 800 nm. As can be seen clearly from the spectrum corresponding to the highest voltage, the emission of

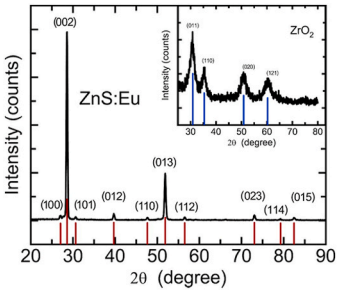

Fig. 2. XRD pattern of the ZnS: Eu phosphor thin film used in the MISIM-ACEL device. The inset shows the XRD pattern of the dielectric ZrO_2 thin films used in the EL device. Both patterns correspond to films deposited on glass substrates.

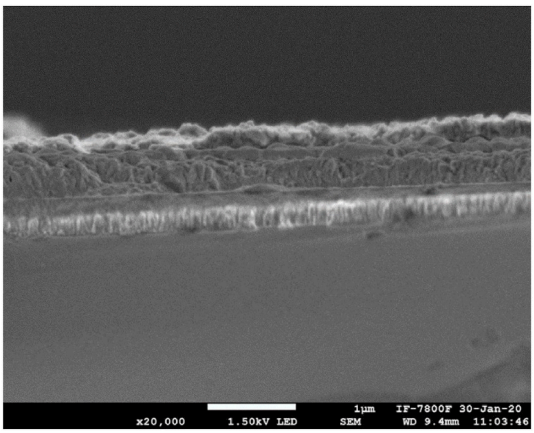

Fig. 3. Cross-sectional image of the MISIM structure, deposited by ultrasonic spray pyrolysis on a glass substrate. The bottom layer is ATO, the layer at the top is the Al electrode.

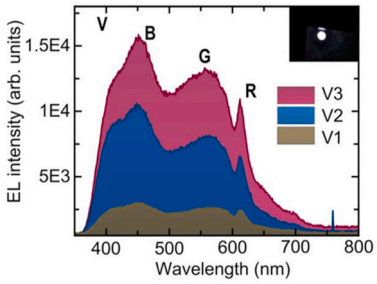

Fig. 4. EL spectra of the MISIM structure fabricated by ultrasonic spray pyrolysis, with ZnS:Eu as a phosphor layer, sandwiched between two ZrO_2 insulating thin films. The RMS voltages are: $V_1 = 56V$, $V_2 = 70V$ *and* $V_3 = 77\ V$. *The inset shows a photograph of the light emitted by the MISIM device under the applied voltage V3.*

the MISIM device is composed of several wide and narrow bands in the visible range 400–700 nm, corresponding to violet (V), blue (B), green (G) and red (R) light, which together produce the white light. Fig. 4 also shows clearly that the overall EL emission rises as the voltage increases from the turn-on voltage (V1) of the device. The inset of Fig. 4 shows a photograph of the white EL emission coming from the surface of the MISIM structure, under the application of the rms voltage V3. Due to AC power supply limitations, we were unable to increase the rms voltage beyond V3 to determine the voltage threshold for device failure. No drop in EL emission was observed after 15 min of maintaining the maximum voltage V3 applied.

The white characteristics of the ACEL device were analyzed employing the Commission Internationale de l'Eclairage (CIE) chromaticity coordinates. According to the CIE, the color characteristics of any light source can be quantitatively described in terms of the three tristimulus values (X, Y, and Z), and the corresponding mathematical relationships with the three-color matching functions $\underline{x}$, $\underline{y}$ and $\underline{z}$. These relationships are the following [42]:

$$X = \int \underline{x} I(\lambda) d\lambda \tag{1}$$

$$Y = \int \underline{y} I(\lambda) d\lambda \tag{2}$$

$$Z = \int \underline{z} I(\lambda) d\lambda \tag{3}$$

where $I(\lambda)$ is the normalized spectral power distribution of the light

source; and λ is the wavelength of the equivalent monochromatic light. As the spectra shown in Fig. 4 are such that $I(\lambda)$ can-not be expressed analytically, the integration must be done by graphic, numerical or mechanical methods. In our case, we used the CIE recommendation that the integration should be carried out by discrete numerical sum, and such computation was made using the datasheet, (http://www.cvrl.org/database/data/cmfs/ciexyz31_1.txt) downloaded from the internet, for the CIE (1931) 2-deg color matching functions, $\underline{x}$, $\underline{y}$ and $\underline{z}$, in steps of 1 nm, and a computer with Origin 2019 and Python. For the representation of the color in the 2D space of the color diagram, the chromaticity coordinates x, y, and z were calculated from the following equations:

$$x = \frac{X}{X+Y+Z}, y = \frac{Y}{X+Y+Z}, z = \frac{Z}{X+Y+Z}. \quad (4)$$

where it must be noticed that, $x + y + z = 1$, and therefore the color can be represented or expressed in terms of two independent coordinates, which are chosen to be (x, y). The CIE coordinates corresponding to the light emitted by the MISIM structure for the three applied voltages are denoted as the sample coordinates (x_s, y_s) and are given in Table 1. Fig. 5 shows the plot of these coordinates onto the CIE diagram that shows the locus coordinates, with labeled hue wavelengths. For the sake of comparison, the white point $(x_i, y_i) = (0.31271, 0.32902)$ of the standard CIE illuminant D65 [43], which corresponds to natural noon daylight, is also plotted onto the CIE diagram of Fig. 5. The varying voltage induces small changes on CIE coordinates, as shown in Fig. 5.

To further evaluate the visual characteristics of the white EL emission as a function of voltage, and how close or far is from the white point corresponding to the illuminant D65, the dominant wavelength and the purity of the light were calculated. The dominant wavelength of a given light or color is the single monochromatic wavelength at which occurs the intersection between the straight line starting from the white point D65, $(x_i, y_i) = (0.31271, 0.32902)$ and passes through the sample point (x_s, y_s) that represents the given light and the locus curve, with labeled hue wavelengths. The color coordinate of this dominant wavelength is denoted as (x_d, y_d). The color purity is defined quantitatively as the ratio between the distance from the illuminant (x_i, y_i) to the point (x_s, y_s) and the distance from (x_i, y_i) to the point (x_d, y_d) corresponding to the dominant wavelength [44]. Thus, the color purity can be calculated using the formula

$$Color\ purity = \frac{\sqrt{(x_s - x_i)^2 + (y_s - y_i)^2}}{\sqrt{(x_d - x_i)^2 + (y_d - y_i)^2}} \times 100\% \quad (5)$$

Fig. 6 shows the CIE coordinates of the white point $(x_i, y_i) = (0.31271, 0.32902)$ (black circle) and the sample point $(x_s, y_s) = (0.28981, 0.31687)$ (black triangle) corresponding to white EL light emitted by the MISIM device at the voltage V3, and the intersection of the straight line with the locus curve at the point $(x_d, y_d) = (0.06599, 0.21037)$ (blue circle) corresponding to the dominant wavelength of 486 nm.

As Fig. 5 and Table 1 show, the white EL light emitted by the MISIM devices under the lowest rms voltage, $V_1 = 56V$, is shifted 5% from the white point toward the blue wavelength of 483 nm, and the shift increases to 10% toward 486 nm as the voltage increases to $V_3 = 77\ V$. This small shift is consistent with the white appearance of the EL light emitted by the ACEL MISIM device (see inset of Fig. 4).

Since, $\underline{y} = V(\lambda)$, is the luminous efficiency function which describes the average spectral sensitivity of human visual perception of bright-

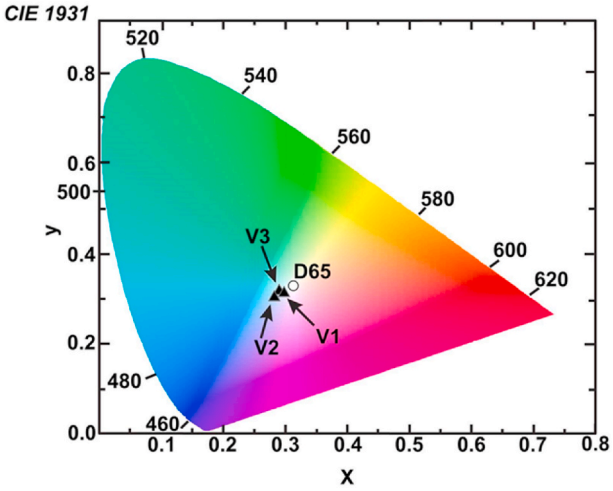

Fig. 5. 1931 CIE chromaticity diagram showing the color space coordinates of the MISIM EL devices operated at $V_1 = 56V$, $V_2 = 70V$ *and* $V_3 = 77\ V$, with respect to the white D65 illuminant. (For interpretation of the references to color in this figure legend, the reader is referred to the Web version of this article.)

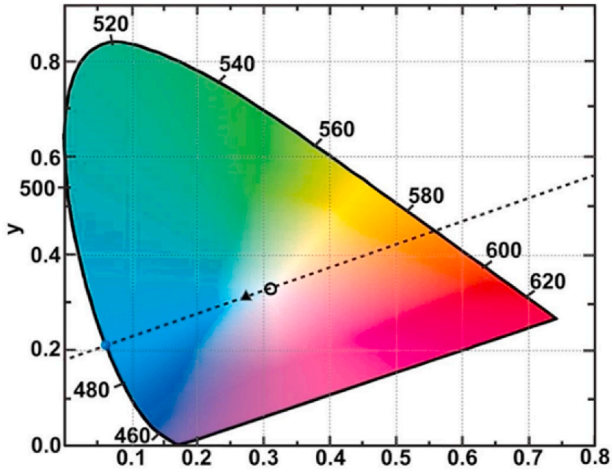

Fig. 6. CIE chromaticity diagram showing the straight line for the determination of the dominant wavelength and purity of the MISIM EL device operated at $V_3 = 77\ V$.

Table 1
CIE chromaticity coordinates of the MISIM EL devices operated at $V_1 = 56V$, $V_2 = 70V$ and $V_3 = 77\ V$. The coordinates of the white D65 illuminant and the corresponding dominant wavelength, color purity and relative luminance are also given in this table.

EL emission	x_s	y_s	Dominant Wavelength (nm) / Color temperature (K)	x_d	y_d	Color purity %	Relative Luminance Y(%)
V1	0.29764	0.31359	483 ~7000	0.07985	0.16525	5.3	74.2
V2	0.28285	0.30323	482 ~9000	0.08082	0.16239	9.6	67.8
V3	0.28981	0.31687	486 ~8000	0.06599	0.21037	10	75.5
D65	x_i 0.31271	y_i 0.32902	–	–	–	0	$Y_0 = 78.5$

ness, the tristimulus value Y expressed by equation (2) is directly proportional to the luminous power or flux of the light, and it is called the relative luminance or brightness. Table 1 shows that the relative luminance Y of the EL device for the three rms applied voltages is close to the relative luminance of the illuminant D65. Fig. 7 shows the normalized EL spectra of the MISIM device along with the normalized spectrum for the illuminant D65. As this figure shows the normalized EL spectra of the MISIM device have a lower contribution of red and infrared emission than the illuminant D65. This is consistent with the slight blue-shift concerning the illuminant that shows the results of the quantitative colorimetric analysis shown in Table 1.

The white EL of these MISIM devices can be explained on the basis of the four mechanisms that occur in this type of ACTFEL device, under the applied electric field, namely: (1) tunnel emission (Fowler-Nordheim type) of electrons from interface states at the interface insulator-phosphor, (2) acceleration of electrons to high energy, (3) impact excitation or ionization of the luminescent centers housed in the phosphor, (4) de-excitation of the excited electrons by radiative and non-radiative recombination [45]. With the change in polarity, these mechanisms are alternated from one to another insulator-phosphor interface. Once the electrons are injected by the step 1, they are accelerated under the action of the electric field (E) inside the phosphor which can be calculated in terms of the applied voltage (V) using the formula [20]: $E = \frac{\varepsilon_i}{\varepsilon_i d_p + 2\varepsilon_p d_i} V$, where ε_i and ε_p are the dielectric constant of the insulating and phosphor layers, respectively, and d_i and d_p are the thicknesses of the insulating and phosphor layers, respectively. Using the average values $\varepsilon_i = 21$ for ZrO_2 and $\varepsilon_p = 5.33$ for ZnS obtained from some references [46,47], and the thickness of the ZrO_2 ($d_i = 150\ nm$) and ZnS ($d_p = 200\ nm$) films in the MISIM device, the resultant electric fields for the three rms applied voltages are $E_1 = 2.0\ MV/\ cm$, $E_2 = 2.5\ MV/cm$ and $E_3 = 2.75\ MV/cm$. If the injected electrons were to accelerate freely under these extremely high electric fields, over a distance x from the interface, they would acquire a kinetic energy, $K = E = eEx$. Under these conditions an electron accelerated, even with the lowest electric field $E_1 = 2.0\ MV/cm$, over a distance $x = 15\ nm$ from the interface, would gain a kinetic energy of $E_1 = 3.0$ eV, which is enough to impact excite electroluminescent centers with significant impact excitation cross-section for energy transitions in the violet-413 nm (3.0 eV), blue- 450 nm (2.75 eV), green-550 nm (2.25 eV) and red-612 nm (2.03 eV) regions. In the more realistic case, where the electrons scatter and lose energy by several high field mechanisms, such as optical and acoustic phonon scattering, impurities scattering, impact ionization and excitation, there is an electron energy distribution which depends on the applied electric field. This electron energy distribution has been calculated for ZnS using Monte Carlo computer simulations, and the simulated results have shown that at the electric field of 2.0 MV/cm, the percentage of electrons with energies between 2.1 eV and 3.2 eV is approximately 54% [48]. Similar results have been found for ZnS using the more simplistic lucky-drift analytical model, which uses the electron mean free path to describe the high field. Still, this model also shows that the energy relaxation length or the distance that the electron propagates before it loses a substantial part of its energy, is 32 nm at 2.0 MV/cm [49]. Once the electrons have been accelerated to the threshold energy, the impact probability is primarily determined by the impact excitation cross-sections of the specific electroluminescent centers [49].

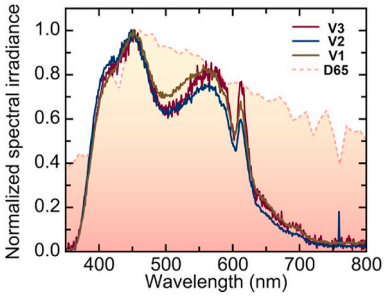

Fig. 7. Normalized EL spectra of D65 illuminant along with that for the MISIM device operated at the three different voltages.

From the above discussion on the electroluminescence mechanisms it is inferred that the EL emission of the MISIM devices is not only determined by the bulk of the phosphor ZnS: Eu film, but is it also significantly influenced by the chemical and electronic properties of the region of the phosphor and the luminescent centers incorporated close to the ZrO_2–ZnS: Eu interfaces. Since the ZnS: Eu film used in the MISIM structure was deposited under the same deposition conditions used in our previous work for depositing these films on glass substrates [40,50], we explain the EL emission band in the blue region as originated from the radiative $4f^6 5d \rightarrow 4f^7$ transitions of Eu^{2+} ions substituting Zn^{2+} in the hexagonal-wurtzite phase of the ZnS: Eu film. At this point it is important to mention that although Eu is commonly incorporated in many luminescent hosts as Eu^{3+}, resulting in red luminescence, the blue luminescence of Eu doped ZnS and borate thin films has been shown to be a strong indication of Eu incorporation as Eu^{2+} in these hosts [40, 50–52]. On the other hand, during the deposition of the ZnS: Eu film onto the ZrO_2 nano-crystalline film, several chemical processes, and homogeneous and heterogeneous reactions can occur, such as, leaching of zirconium from the ZrO_2 film, and the formation of ZnO sublayers and surface functionalization with the ZnS adjacent monolayers [53–55], giving rise to incorporation of some Eu impurities as Eu^{3+} in the ZnO and ZnS growing layers and on the surface of the ZrO_2 nano-crystalline film. During the deposition of the ZrO_2 onto the ZnS:Eu film, it is also feasible the formation of ZnO sublayers due to surface oxidation of the ZnS:Eu film, and the incorporation of Eu^{3+} on the ZnO surface growing layer and on the surface of the ZrO_2 nanocrystals. This is consistent with the fact that the prominent peaks and edges in the red region of the three EL spectra shown in Fig. 4, correspond quite well with intra-ion $^5D_0 \rightarrow {}^7F_J$ (J = 0, 1, 2, 3, 4) 4f-transitions of Eu^{3+} ions incorporated in ZnS, ZnO and ZrO_2 nanocrystals or thin films [33,42,56–58], in the region of the ZnS: Eu phosphor film, close to the ZrO_2–ZnS:Eu interface.

It is well known that the corresponding ranges of wavelengths of these Eu^{3+} transitions in different compounds are: 570–585 nm (J = 0), 585–600 nm (J = 1), 610–630 nm (J = 2), 640–660 nm (J = 3), 680–710 nm (J = 4), where the $^5D_0 \rightarrow {}^7F_2$ transition at 612 nm is the dominant one, but the intensity and width of this and other transitions are dependent on the chemical environment [1,59]. Since the doping of the ZnS and ZnO sublayers with Eu^{3+} produces intrinsic defects such as interstitials and vacancies of zinc and sulfur, and oxygen vacancies, the broad green-yellow emission that exhibit the EL spectra of Fig. 4 may also be assigned to radiative transitions between the different defects created in the ZnS and ZnO sublayers [28–30,56,60]. Studies on the electronic interface properties of a ZnO monolayer on a ZnS sublayer have shown that the surface functionalization of these two direct bandgap materials with bandgaps larger than 3.4 eV, results in an effective surface band gap narrowing from 3.4 eV until 2.8 eV [54]. Based on this, we can assume that photons generated from ZnS–ZnO inter-band transitions, could contribute to the prominent edge observed in the UV region of the spectra of the ACTFEL devices shown in Fig. 4.

4. Conclusions

In summary, we have demonstrated a MISIM-ACTFEL device with white emission fabricated by ultrasonic spray pyrolysis using ZnS: Eu films as semiconducting phosphor layer and ZrO_2 as insulating layers. The device exhibited white EL emission slightly blueish. The shade of the white light was determined from the CIE chromaticity coordinates, which resulted 5%–10% close to the illuminant D65. The variation of the applied voltage induces small changes in CIE coordinates. The White EL emission of these MISIM devices is attributed to the electron-impact excitation and subsequent relaxation of the excited levels of Eu^{2+} and

Eu^{3+} impurities, and intrinsic point defect levels in the sublayer regions adjacent to the ZrO_2–ZnS:Eu interfaces.

CRediT authorship contribution statement

Martha Judith Rivera-Medina: Investigation, Methodology, Visualization, Writing – original draft. **Angélica Carrillo-Verduzco:** Validation, Investigation. **Arturo Rodríguez-Gómez:** Validation, Investigation. **Maria Antonietta Loi:** Supervision, Writing – review & editing. **Juan Carlos Alonso-Huitrón:** Supervision, Conceptualization, Methodology, Resources, Formal analysis, Writing – review & editing.

Declaration of competing interest

The authors declare that they have no known competing financial interests or personal relationships that could have appeared to influence the work reported in this paper.

Acknowledgment

We want to thank A. Tejeda for X-ray diffraction technical support, and B. Juárez García, and E. A. González Villa for the provision of the Python program for colorimetry analysis. The authors are also grateful to Fis. Roberto Hernández, Dr. Samuel Tehuacanero Cuapa, Dr. Carlos Magaña, and Mtro. Manuel Aguilar Franco for technical assistance in the SEM analysis. This research work received financial support from the project PAPIIT-UNAM, number IN109020. Authors acknowledge and appreciate the invaluable labor and courage of all those who, during the tragic COVID-19 pandemic, expose their lives to keep doing first necessity activities for the good of all society.

References

[1] J. Rosa, M.J. Heikkilä, M. Sirkiä, S. Merdes, Red Y2O3:Eu-based electroluminescent device prepared by atomic layer deposition for transparent display applications, Materials 14 (2021) 1505, https://doi.org/10.3390/ma14061505.
[2] C. Qi, Y. Zhou, X. Tao, H. Chen, Y. Ouyang, X. Mo, Toward near-white electroluminescence with enhanced blue emission from carbon dots in PEDOT: PSS/ZnO organic/inorganic hybrid heterojunctions, J. Lumin. 224 (2020), 117230, https://doi.org/10.1016/j.jlumin.2020.117230.
[3] D. Zhao, J. Qian, S. Ye, Y. Li, J. Wang, White electroluminescent devices based on hybrid structure with quantum dot color convertors, Opt Express 28 (2020) 14176–141185, https://doi.org/10.1364/oe.382220.
[4] J. Zhang, B. Ren, S. Deng, J. Huang, L. Jiang, D. Zhou, X. Zhang, M. Zhang, R. Chen, F. Yeung, H. Kwok, P. Xu, G. Li, Voltage-dependent multicolor electroluminescent device based on halide perovskite and chalcogenide quantum-dots emitters, Adv. Funct. Mater. 30 (2020), 1907074, https://doi.org/10.1002/adfm.201907074.
[5] J. Zhang, H. Tsai, W. Nie, B. Hu, Enabling AC electroluminescence in quasi-2D perovskites by uniformly arranging different-n-value nanoplates to allow bidirectional charge transport, Nanomater. Energy 79 (2020), 105413, https://doi.org/10.1016/j.nanoen.2020.105413.
[6] C. Ruan, Y. Zhang, M. Lu, C. Ji, C. Sun, X. Chen, H. Chen, V.L. Colvin, W.W. Yu, White light-emitting diodes based on AgInS2/ZnS quantum dots with improved bandwidth in visible light communication, Nanomaterials 6 (2016) 1–8, https://doi.org/10.3390/nano6010013.
[7] Y. He, M. Zhang, N. Zhang, D. Zhu, C. Huang, L. Kang, X. Zhou, M. Hu, J. Zhang, Paper-based ZnS:Cu alternating current electroluminescent devices for current humidity sensors with high-linearity and flexibility, Sensors 19 (2019) 4607, https://doi.org/10.3390/s19214607.
[8] J. Song, H. Lee, E.G. Jeong, K.C. Choi, S. Yoo, Organic light-emitting diodes: pushing toward the limits and beyond, Adv. Mater. 32 (2020), 1907539, https://doi.org/10.1002/adma.201907539.
[9] M.A. Johar, H.G. Song, A. Waseem, M.A. Hassan, I.V. Bagal, Y.H. Cho, S.W. Ryu, Universal and scalable route to fabricate GaN nanowire-based LED on amorphous substrate by MOCVD, Appl. Mater. Today. 19 (2020), 100541, https://doi.org/10.1016/j.apmt.2019.100541.
[10] Y. Shirasaki, G.J. Supran, M.G. Bawendi, V. Bulović, Emergence of colloidal quantum-dot light-emitting technologies, Nat. Photonics 7 (2013) 13–23, https://doi.org/10.1038/nphoton.2013.328.
[11] L. Wang, L. Xiao, H. Gu, H. Sun, Advances in alternating current electroluminescent devices, Adv. Opt. Mater. 7 (2019) 1–30, https://doi.org/10.1002/adom.201801154.
[12] J.D. Slinker, J. Rivnay, J.A. Defranco, D.A. Bernards, A.A. Gorodetsky, S.T. Parker, M.P. Cox, R. Rohl, G.G. Malliaras, S. Flores-Torres, H.D. Abruña, Direct 120 V, 60 Hz operation of an organic light emitting device, J. Appl. Phys. 99 (2006), https://doi.org/10.1063/1.2186031.
[13] J. Junpeng, I.F. Perepichka, J. Bai, D. Hu, X. Xu, M. Liu, T. Wang, C. Zhao, H. Meng, W. Huang, Three-phase electric power driven electoluminescent devices, Nat. Commun. 12 (2021) 1–11, https://doi.org/10.1038/s41467-020-20265-2.
[14] A. Perumal, B. Lüssem, K. Leo, High brightness alternating current electroluminescence with organic light emitting material, Appl. Phys. Lett. 100 (2012), https://doi.org/10.1063/1.3692776.
[15] G. Liang, H. Hu, L. Liao, Y. He, C. Ye, Highly flexible and bright electroluminescent devices based on Ag nanowire electrodes and top-emission structure, Adv. Electron. Mater. 3 (2017) 1–7, https://doi.org/10.1002/aelm.201600535.
[16] E. Torres Alonso, G. Karkera, G.F. Jones, M.F. Craciun, S. Russo, Homogeneously bright, flexible, and foldable lighting devices with functionalized graphene electrodes, ACS Appl. Mater. Interfaces 8 (2016) 16541–16545, https://doi.org/10.1021/acsami.6b04042.
[17] C. Tsakonas, S. Wakeham, W.M. Cranton, M. Thwaites, G. Boutaud, C. Farrow, D. C. Koutsogeorgis, R. Ranson, Transparent and flexible thin film electroluminescent devices using HiTUS deposition and laser processing fabrication, IEEE J. Electron Devices Soc. 4 (2016) 22–29, https://doi.org/10.1109/JEDS.2015.2497086.
[18] M.R. Fernández, E.Z. Casanova, I.G. Alonso, Review of display technologies focusing on power consumption, Sustain. Times 7 (2015) 10854–10875, https://doi.org/10.3390/su70810854.
[19] Y.A. Ono, Electroluminescent Displays, World Scientific Publishing Co. Pte. Ltd., Singapore, 1995.
[20] P.D. Rack, P.H. Holloway, The structure, device physics, and material properties of thin film electroluminescent displays, Mater. Sci. Eng. R Rep. 21 (1998) 171–219, https://doi.org/10.1016/S0927-796X(97)00010-7.
[21] P.F. Smet, I. Moreels, Z. Hens, D. Poelman, Luminescence in sulfides: a rich history and a bright future, Materials 3 (2010) 2834–2883, https://doi.org/10.3390/ma3042834.
[22] V. Lahariya, M. Ramrakhiani, Luminescence Study on Mn,Ni Co-doped Zinc Sulfide Nanocrystals, Luminescence, 2020, pp. 1–10, https://doi.org/10.1002/bio.3802.
[23] C.D. Brubaker, K.N. Newcome, G.K. Jennings, D.E. Adams, 3D-Printed alternating current electroluminescent devices, J. Mater. Chem. C. 7 (2019) 5573–5578, https://doi.org/10.1039/c9tc00619b.
[24] Y. Zuo, X. Shi, X. Zhou, X. Xu, J. Wang, P. Chen, X. Sun, H. Peng, Flexible color-tunable electroluminescent devices by designing dielectric-distinguishing double-stacked emissive layers, Adv. Funct. Mater. 30 (2020) 1–9, https://doi.org/10.1002/adfm.202005200.
[25] E.B. Ramírez, M. Bizarro, J.C. Alonso, Synthesis and characterization of thin film electroluminescent devices all-prepared by ultrasonic spray pyrolysis, Thin Solid Films 548 (2013) 255–258.
[26] S. Khan, H.Y. Ahn, J.S. Han, B.K. Ju, S.Y. Lee, H.S. Jang, J.Y. Byun, S.H. Cho, Luminescent silica films prepared using perhydropolysilazane and Mn-doped ZnS nanophosphors, Appl. Surf. Sci. 511 (2020), 145441, https://doi.org/10.1016/j.apsusc.2020.145441.
[27] B. Pejjai, V.R. Minnam Reddy, K. Seku, T.R.R. Kotte, C. Park, Chemical bath deposition of Mn-doped ZnS thin films using greener complexing agents: effect of Mn-doping on the optical properties, Optik 130 (2017) 608–618, https://doi.org/10.1016/j.ijleo.2016.10.083.
[28] W. Zhang, X. Zeng, H. Liu, J. Lu, Synthesis and investigation of blue and green emissions of ZnS ceramics, J. Lumin. 134 (2013) 498–503, https://doi.org/10.1016/j.jlumin.2012.07.039.
[29] X. Wang, J. Shi, Z. Feng, M. Li, C. Li, Visible emission characteristics from different defects of ZnS nanocrystals, Phys. Chem. Chem. Phys. 13 (2011) 4715–4723, https://doi.org/10.1039/c0cp01620a.
[30] Y. Li, L. Zhang, K. Kisslinger, Y. Wu, Green phosphorescence of zinc sulfide optical ceramics, Opt. Mater. Express 4 (2014) 3212–3220, https://doi.org/10.1364/OME.4.001140.
[31] D. Li, B.L. Clark, D.A. Keszler, P. Keir, J.F. Wager, Color control in sulfide phosphors: turning up the light for electroluminescent displays, Chem. Mater. 12 (2000) 268–270, https://doi.org/10.1021/cm9904234.
[32] M. Aozasa, H. Chen, K. Ando, ZnS:Eu thin film electroluminescent devices prepared by r.f. magnetron sputtering, Thin Solid Films 199 (1991) 129–138, https://doi.org/10.1016/0040-6090(91)90059-7.
[33] M.K. Jayaraj, C.P.G. Vallabhan, AC thin film electroluminescent devices with rare earth doped ZnS, J. Electrochem. Soc. 138 (1991) 1512–1516, https://doi.org/10.1149/1.2085817.
[34] M. Leskelä, M. Mattinen, M. Ritala, Review Article: atomic layer deposition of optoelectronic materials, J. Vac. Sci. Technol. B. 37 (2019), 030801, https://doi.org/10.1116/1.5083692.
[35] Q.Z. Gao, J. Mita, T. Tsuruoka, M. Kobayashi, K. Kawamura, High luminance white EL devices using SrS:Ce,Eu,K films deposited in a H2 atmosphere, J. Cryst. Growth 117 (1992) 983–986, https://doi.org/10.1016/0022-0248(92)90897-R.
[36] Luminescent materials and applications, in: A. Kitai (Ed.), Lumin. Mater. Appl., 2008, pp. 223–248.
[37] E.I. Anila, M.K. Jayaraj, Low temperature deposition of SrS:Cu,F ACTFEL device by electron beam evaporation, J. Lumin. 130 (2010) 2180–2183, https://doi.org/10.1016/j.jlumin.2010.06.016.
[38] K. Ohmi, K. Yamabe, H. Fukada, T. Fujiwara, S. Tanaka, H. Kobayashi, Blue SrS:Cu thin-film electroluminescent devices grown by hot-wall deposition using successive source supply, Appl. Phys. Lett. 73 (1998) 1889–1891, https://doi.org/10.1063/1.122316.
[39] S. Tanaka, H. Kobayashi, H. Sasakura, Y. Hamakawa, Evidence for the direct impact excitation of Mn centers in electroluminescent ZnS:Mn films, J. Appl. Phys. 47 (1976) 5391–5393, https://doi.org/10.1063/1.322567.

[40] M.J. Rivera-Medina, J. HernándezHern, J.L. BoldúBold, J. Barreto-RenteríaRentería, J.M. HernándezHern, V. Jancik, J.C. Alonso-HuitrónHuitr, Synthesis of europium-doped ZnS nano-crystalline thin films with strong blue photoluminescence †, RSC Adv. 6 (2016) 107613–107621, https://doi.org/10.1039/c6ra24300b.

[41] J.C. Alonso, F.A. Pulgarín, B.M. Monroy, A. Benami, M. Bizarro, A. Ortiz, Visible electroluminescence from silicon nanoclusters embedded in chlorinated silicon nitride thin films, Thin Solid Films 518 (2010) 3891–3893, https://doi.org/10.1016/j.tsf.2009.11.060.

[42] S.J. Yoon, J.W. Pi, K. Park, Structural and photoluminescence properties of solution combustion-processed novel ZrO2 doped with Eu3+ and Al3+, Dyes Pigments 150 (2018) 231–240, https://doi.org/10.1016/j.dyepig.2017.12.012.

[43] A.K.R. Choudhury, Principles of Colour and Appearance Measurement, Woodhead Publishing Limited, Amsterdam, 2014.

[44] Y. Shi, Y. Wen, M. Que, G. Zhu, Y. Wang, Structure, photoluminescent and cathodoluminescent properties of a rare-earth free red emitting β-Zn 3 B 2 O 6 :Mn 2+ phosphor, Dalton Trans. 43 (2014) 2418–2423, https://doi.org/10.1039/C3DT52405A.

[45] W.A.D.M. Jayathilaka, A. Chinnappan, J.N. Tey, J. Wei, S. Ramakrishna, Alternative current electroluminescence and flexible light emitting devices, J. Mater. Chem. C. 7 (2019) 5553–5572, https://doi.org/10.1039/c9tc01267b.

[46] D. Panda, T.Y. Tseng, Growth, dielectric properties, and memory device applications of ZrO2 thin films, Thin Solid Films 531 (2013) 1–20, https://doi.org/10.1016/j.tsf.2013.01.004.

[47] A. Goswami, A.P. Goswami, Dielectric and optical properties of ZnS films, Thin Solid Films 16 (1973) 175–185, https://doi.org/10.1016/0040-6090(73)90166-1.

[48] K. Bhattacharyya, S.M. Goodnick, J.F. Wager, Monte Carlo simulation of electron transport in alternating-current thin-film electroluminescent devices, J. Appl. Phys. 73 (1993) 3390–3395, https://doi.org/10.1063/1.352938.

[49] E. Bringuier, Impact excitation in ZnS-type electroluminescence, J. Appl. Phys. 70 (1991) 4505–4512, https://doi.org/10.1063/1.349085.

[50] V.H. López-Lugo, M.J. Rivera-Medina, J.C. Alonso-Huitrón, Quantitative assessing of crystal field, nephelauxetic, and Stokes shift effects on the blue luminescence of Eu 2+ ions incorporated in ZnS films, Mater. Res. Express 8 (2021), 036406, https://doi.org/10.1088/2053-1591/abee00.

[51] J. Hao, M. Cocivera, Luminescent characteristics of blue-emitting Sr2B5O9Cl: Eu thin-film phosphors, Appl. Phys. Lett. 79 (2001) 740–742, https://doi.org/10.1063/1.1391410.

[52] J. Hao, J. Gao, M. Cocivera, Tuning of the blue emission from europium-doped alkaline earth chloroborate thin films activated in air, Appl. Phys. Lett. 82 (2003) 2778–2780, https://doi.org/10.1063/1.1569048.

[53] F. Forte, L. Yurramendi, J.L. Aldana, B. Onghena, K. Binnemans, Integrated process for the recovery of yttrium and europium from CRT phosphor waste, RSC Adv. 9 (2019) 1378–1386, https://doi.org/10.1039/C8RA08158A.

[54] J. Lahiri, M. Batzill, Surface functionalization of ZnO photocatalysts with monolayer ZnS, J. Phys. Chem. C 112 (2008) 4304–4307, https://doi.org/10.1021/jp7114109.

[55] T.T. Ngoc Van, A.S. Ansari, B. Shong, Surface chemical reactions during atomic layer deposition of ZnO, ZnS, and Zn(O,S), J. Vac. Sci. Technol. A. 37 (2019), 020909, https://doi.org/10.1116/1.5079247.

[56] H.V.S. Pessoni, L.J.Q. Maia, A. Franco, Eu-doped ZnO nanoparticles prepared by the combustion reaction method: structural, photoluminescence and dielectric characterization, Mater. Sci. Semicond. Process. 30 (2015) 135–141, https://doi.org/10.1016/j.mssp.2014.09.039.

[57] Y.P. Du, Y.W. Zhang, L.D. Sun, C.H. Yan, Efficient energy transfer in monodisperse Eu-doped ZnO nanocrystals synthesized from metal acetylacetonates in high-boiling solvents, J. Phys. Chem. C 112 (2008) 12234–12241, https://doi.org/10.1021/jp802958x.

[58] S. Gao, H. Zhang, R. Deng, X. Wang, D. Sun, G. Zheng, Engineering white light-emitting Eu-doped ZnO urchins by biopolymer-assisted hydrothermal method, Appl. Phys. Lett. 89 (2006) 67–70, https://doi.org/10.1063/1.2357031.

[59] K. Binnemans, Interpretation of europium(III) spectra, Coord. Chem. Rev. 295 (2015) 1–45, https://doi.org/10.1016/j.ccr.2015.02.015.

[60] A.L. Curcio, L.F. da Silva, M.I.B. Bernardi, E. Longo, A. Mesquita, Nanostructured ZnS:Cu phosphor: correlation between photoluminescence properties and local structure, J. Lumin. 206 (2019) 292–297, https://doi.org/10.1016/j.jlumin.2018.10.073.